

Charge to Spin Conversion in van der Waals Metal NbSe₂

Anamul Md. Hoque¹, Bing Zhao¹, Dmitrii Khokhriakov¹, Prasanta Muduli², Saroj P. Dash^{1,3*}

¹*Department of Microtechnology and Nanoscience, Chalmers University of Technology, SE-41296, Göteborg, Sweden*

²*Department of Physics, Indian Institute of Technology Madras, Chennai 600036, India*

³*Graphene Center, Chalmers University of Technology, SE-41296, Göteborg, Sweden*

Abstract:

Quantum materials with a large charge current-induced spin polarization are promising for next-generation all-electrical spintronic science and technology. Van der Waals metals with high spin-orbit coupling and novel spin textures have attracted significant attention for an efficient charge to spin conversion process. Here, we demonstrate electrical generation of spin polarization in NbSe₂ up to room temperature. To probe the current-induced spin polarization in NbSe₂, we used a graphene-based non-local spin-valve device, where the spin-polarization in NbSe₂ is efficiently injected and detected using non-local spin-switch and Hanle spin precession measurements. A significantly higher charge-spin conversion in NbSe₂ is observed at a lower temperature, below the superconducting transition temperature $T_c \sim 7$ K of NbSe₂. However, the charge-spin conversion signal could only be observed with a higher bias current above the superconducting critical current, limiting the observation of signal only to the non-superconducting state of NbSe₂. Systematic measurements provide the possible origins of the spin polarization to be predominantly due to the spin Hall effect or Rashba-Edelstein effect in NbSe₂, considering different symmetry allowed charge-spin conversion processes.

Keywords: Nonmagnetic spin source, current-induced spin polarization, NbSe₂, graphene, spin Hall effect, Rashba Edelstein effect, spintronics, spin-valve, Hanle

Corresponding author: saroj.dash@chalmers.se

Introduction

Two-dimensional (2D) materials and their van der Waals (vdW) heterostructures have become attractive platforms to explore numerous physical phenomena, primarily associated with spin-orbit coupling (SOC), exotic superconductivity, and magnetism for next-generation novel electronic devices^{1–3}. 2D transition metal dichalcogenides (TMDCs) are ideal hosts for realizing spin-polarized electronic states due to the high SOC accompanied with broken symmetries (structural, rotational, translational, etc.) in the crystal structure^{4–7}. Recently, van der Waals materials have paved the way for utilizing various charge-to-spin interconversion (CSC) processes owing to fascinating electronic band structures and lower crystal symmetries^{4,8–10}. For example, both conventional and unconventional charge-to-spin interconversion effects and out-of-plane spin-orbit torque (SOT) components are observed in semimetals such as WTe_2 , MoTe_2 , and NbSe_2 up to room temperature^{11–18}. Interestingly, the 2D materials can be fabricated in vdW heterostructures with atomically clean interfaces without adulterating their distinctive electronic properties, which provide new routes for band structure engineering and proximity induced SOC^{19–22}. For instance, heterostructures of graphene with 2D semiconductors, semimetals, and topological insulators have shown unprecedented gate tunable CSC processes and novel spin textures^{17,23–31}.

It is known that 2H NbSe_2 is a vdW layered metallic TMDC with superconducting (SC) behaviour below a critical temperature $T_c \approx 7\text{K}$ ^{32–34}. It is expected that the CSC effects can be enhanced in the SC state mediated by quasiparticles with higher spin lifetimes^{3,35,36}. Interestingly, NbSe_2 in the normal state also has enormous prospects in the CSC process, triggered by high SOC of the Nb 4*d* orbital and breaking of symmetries with higher electrical conductivities than semiconductive and semimetallic TMDCs¹¹. NbSe_2 also exhibits Ising-type SOC similar to the intrinsic Zeeman field, which results in unconventional spin textures^{37–39}. Recently in the NbSe_2 and Permalloy bilayer system, current-induced spin-orbit torque (SOT) measurements demonstrated a large anti-damping torque owing to strain-induced symmetry breaking¹¹. Furthermore, spin- and angle-resolved photoemission spectroscopy (ARPES) also reveals that the electronic band structure of NbSe_2 in the normal state hosts a strong momentum-dependent spin polarization at Fermi level^{40,41}. Such fascinating spin-dependent electronic properties in NbSe_2 are highly desirable to create current-induced spin polarization.

Here, we demonstrate the electronic generation of spin polarization in NbSe_2 up to room temperature owing to the efficient charge to spin conversion (CSC) process. The engendered spin polarization in NbSe_2 is efficiently injected into the graphene spin-channel in the vdW heterostructure spin-valve device and detected by a ferromagnet (FM) using non-local spin-switch and Hanle spin-precession measurements up to room temperature. A significantly higher CSC signal in NbSe_2 is observed at a lower temperature, however, in the non-superconducting regime. These findings demonstrate NbSe_2 to be a metallic spin source up to room temperature with efficient control of spin polarization by the bias current magnitude, which can be pivotal for future energy-efficient all-electric spin-based technologies^{9,10,42,43}.

Results

Fabrication of NbSe_2 -graphene heterostructure device

To detect the CSC properties in NbSe_2 , we fabricated NbSe_2 -graphene vdW heterostructure devices. We used chemical vapor deposited (CVD) graphene as a spin channel material, due to its excellent spin transport property arising from low SOC and hyperfine interactions^{44–46}. Most interestingly, it was demonstrated that graphene can make a very good vdW heterostructure with other 2D materials^{20,47,48}. Figure 1a presents the schematic of the NbSe_2 -graphene vdW heterostructure device along with ferromagnetic (FM) contacts to characterize the spin transport properties in the heterostructure (see the device fabrication part for details). A scanning electron microscopic (SEM) image of a fabricated device

consisting of CVD graphene, multilayer NbSe₂ flake, and multiple FM contacts is shown in Fig.1(b). An optical micrograph and atomic force microscopic (AFM) image of the corresponding device has been shown in Fig. S1. This device consists of 23 nm NbSe₂ on top of monolayer CVD graphene with TiO₂/Co as ferromagnetic tunnel contacts. The interface resistance between NbSe₂-graphene is found to be 50 Ω, the FM contact resistance is 12kΩ and the field-effect mobility (μ) of the graphene channel is $\approx 2000\text{cm}^2\text{V}^{-1}\text{s}^{-1}$ (see Fig. S2).

As a high SOC material, NbSe₂ can give rise to current-induced in-plane (y-axis) spin polarization via conventional spin Hall effect (shown in Fig. 1c), where charge current (I_c) along the x-axis creates a transverse spin current (I_s) along the z-axis^{15,18}. Furthermore, high SOC in conjunction with breaking inversion symmetry along the z-axis due to two different atoms in layered NbSe₂ crystal can result in Rashba spin splitting in the band structure with helical spin texture with opposite spin-subbands, as shown in Fig. 1(d). Upon application of an electric field (E), hence the charge current can shift the helical Fermi surface in the k-space and create net spin polarization via the Rashba-Edelstein effect. The created spin polarization in NbSe₂ can be injected into a graphene spin-channel in VdW heterostructure and detected by non-local measurement geometry to realize a pure spin signal.

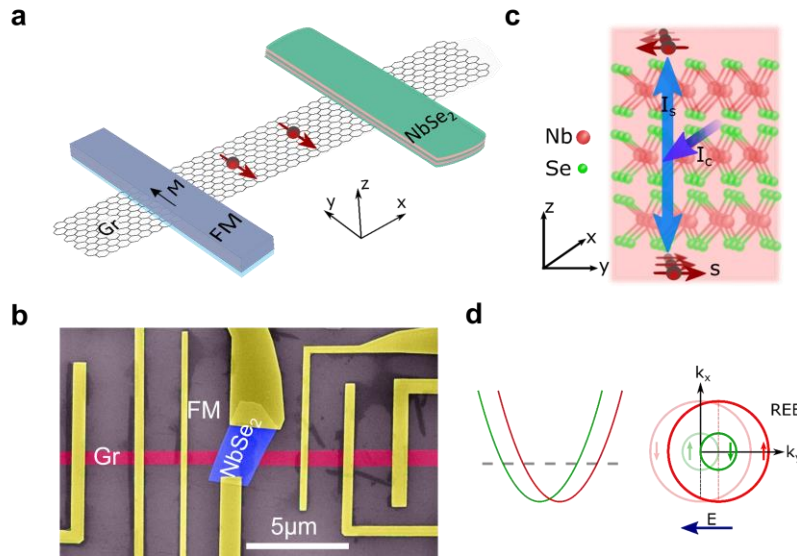


Figure 1. The device design of NbSe₂-graphene heterostructure. (a) Schematic of NbSe₂-graphene heterostructure, where NbSe₂ creates non-equilibrium spin polarization and injects spin-polarized electrons into graphene spin-channel, which is detected by an FM (TiO₂/Co) contacts in non-local measurement geometry. (b) Colored scanning electron microscopic (SEM) image of a fabricated device consisting of CVD graphene (Gr), multilayer NbSe₂ flake (blue), and multiple FM contacts (yellow) to characterize spin transport properties in the heterostructure. The scale bar (white line) in the image is 5 μm. (c) Schematic illustration of charge to spin conversion process due to conventional spin Hall effect in NbSe₂, where charge current (I_c) engenders a transverse spin current (I_s). (d) Charge current from the applied electric field (E) induced spin polarization due to the Rashba-Edelstein effect (REE) at the Fermi surface in spin-split bands of a high spin-orbit coupling system.

Material properties and superconductivity of NbSe₂

At first, high-quality crystal structures of the materials were ensured by Raman spectroscopy. The Raman spectrum of single-layer CVD graphene (top panel) and exfoliated multilayer NbSe₂ (bottom panel) using 638 nm LASER have been presented in Fig. 2a. The Raman spectra of graphene confirm high-quality graphene crystal since almost no defect-induced D peak is observed. Furthermore, the higher intensity of the 2D peak at 2645 cm⁻¹ than that of the G peak at 1590 cm⁻¹ indicates the growth of single-layer graphene⁴⁹. In the case of NbSe₂, the characteristic out-of-plane phonon mode A1g peak for multilayer 2H NbSe₂ is observed at 230 cm⁻¹^{50,51} (see Fig. 2a bottom panel).

We started with investigating the superconducting properties of exfoliated multilayer NbSe₂ flake by measuring the temperature dependence of longitudinal resistance in four-terminal measurement (4T) geometry, as shown in Fig. 2b. The device picture and measurement geometry are shown in the insets of Fig. 2b. We used 1 μ A of DC bias current and the superconducting critical temperature (T_c) in this flake is found to be 6.8K. The four-probe IV measurement with DC bias current and corresponding differential resistance (dV/dI) as a function of the bias current at 3K for the NbSe₂ flake are shown in Fig. 2c and 2d, respectively. The nonlinear IV is due to superconductive properties in NbSe₂ and from the dV/dI plot, we can estimate the critical current density, $J_{c, NbSe_2} = 0.7 \times 10^6$ A/cm² for the multilayer NbSe₂ at 3K, consistent with the recent study⁵². The room temperature IV measurement (shown in Fig. S3b, c) is in agreement with the metallic properties of NbSe₂. Raman spectroscopies, together with the presence of superconducting transition in NbSe₂ confirm good-quality materials are used in the heterostructure.

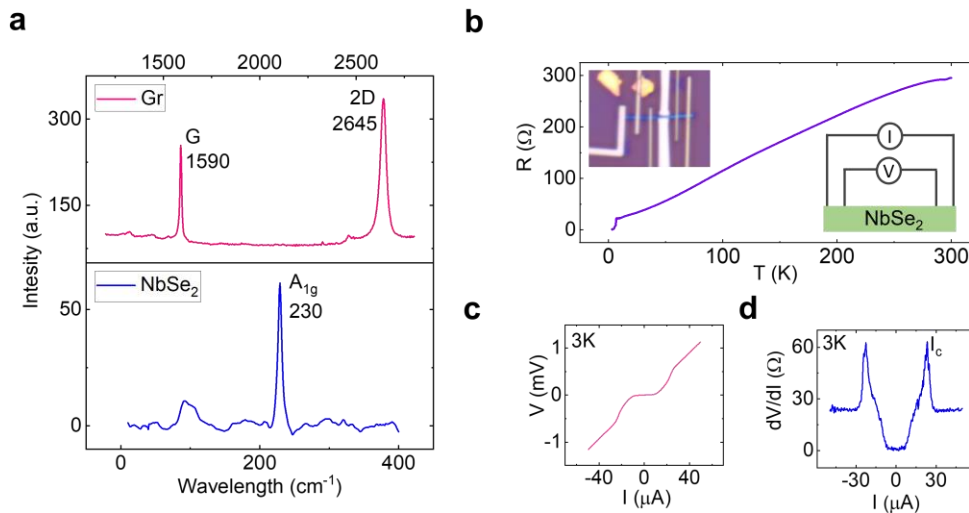


Figure 2. Materials characteristics of NbSe₂ and graphene. (a) Raman spectrum of single-layer CVD graphene (top panel) and exfoliated multilayer NbSe₂ (bottom panel) using 638 nm LASER. (b) Temperature dependence of the longitudinal resistance of multilayer NbSe₂ flake, where superconducting critical temperature (T_c) is around 6.8K is evident. Insets are the device picture (top) and four-terminal measurement geometry. (c,d) The four-probe IV measurements and corresponding differential resistance as a function of the bias current in the multilayer NbSe₂ flake at 3K.

Charge-spin conversion in NbSe₂

In order to investigate the charge-spin conversion (CSC) effect in NbSe₂, a charge current is applied in a multilayer NbSe₂ flake to create a non-equilibrium spin polarization on its surface. The spins are injected into the graphene channel and finally detected by an FM contact in non-local measurement geometry. Figure 3a shows a schematic illustration of the measurement geometry used to detect the CSC effect in NbSe₂ along with the axis orientation and corresponding spin (s), charge current (I_c) and spin components (I_s). According to our measurement geometry in Fig. 3a by considering conventional SHE in NbSe₂, a charge current along x-axis can create an out-of-plane (z-axis) spin current, which renders spin polarization along y-axis. It is worth mentioning that the spin diffusion current in graphene spin channel is along x-axis in our measurement geometry with spin orientation towards y-axis after spin polarization is created in NbSe₂ and injected into graphene. In our experiments, we measure the non-local voltage at the FM contact (left nearest contact to the NbSe₂ flake, shown in Fig. 1b) by applying varying magnetic fields along with the B_y and B_z directions, respectively. A varying magnetic field along the magnetic easy axis (y-axis) switches the magnetization of the FM contact and renders a switching signal which detects non-equilibrium in-plane spin in graphene injected from the NbSe₂ flake. The spin-switch signal presented in Fig. 3b is measured with $I = 400 \mu$ A at $V_g = -40$ V (the up and down magnetic sweep directions are indicated by arrows). The amplitude of the signal estimated from the change in non-local

resistance corresponding to the opposite magnetization of the FM contact is about, $\Delta R_{nl} = 1.77 \pm 0.6$ m Ω .

Furthermore, an out-of-plane varying magnetic field (B_z) in our measurement geometry should render a Hanle spin precession signal, which unequivocally confirms the CSC process in the NbSe₂ and spin transport in the graphene spin channel. Figure 3(c) shows the manifested Hanle spin signal measured with $I = +420$ μ A and $V_g = -40$ V while injecting spin from NbSe₂ into the graphene channel along with the fitting to equation S1. We have estimated the spin lifetime, $\tau_s = 23 \pm 6$ ps and spin diffusion length, $\lambda_s = \sqrt{\tau_s D_s} = 0.65 \pm 0.05$ μ m, considering the channel length $L = 2.4$ μ m (distance between the center of the NbSe₂ flake to the center of the detector's FM electrode). Moreover, the spin transport in the pristine CVD graphene at different gate voltages is shown in S4, where spin lifetime is estimated to be around 150 ps. In NbSe₂-graphene heterostructure, the lower τ_s in graphene spin channel after spin is injected from NbSe₂ can be attributed to the influence of long-range disorders, lattice deformation, and extrinsic interstitials in the graphene crystal that acts as spin-defect centers. These imperfections might be introduced during processing CVD graphene, NbSe₂ transfer, and device fabrication processes⁵³. Additionally, spin absorption by NbSe₂ can also give rise to lower τ_s because of the transparent NbSe₂-graphene interface. Interestingly, we observe only symmetric Hanle component, although the NbSe₂ flake in our device is at an angle to the graphene spin channel⁵⁴. Furthermore, any contribution from the spin injection from the FM contact on NbSe₂ can be eliminated from the spin switch signal, because the influence of and FM magnetization would have manifested typical spin valve signal (as presented in Fig. S4a) with double spin-valve switching while sweeping B_y . Besides, Hanle measurement rules out any effect of stray fields from the detector FM contact on the manifested CSC signals, since the stray Hall effect would have rendered linear Hall signal for an out-of-plane field (B_{\perp})⁵⁵.

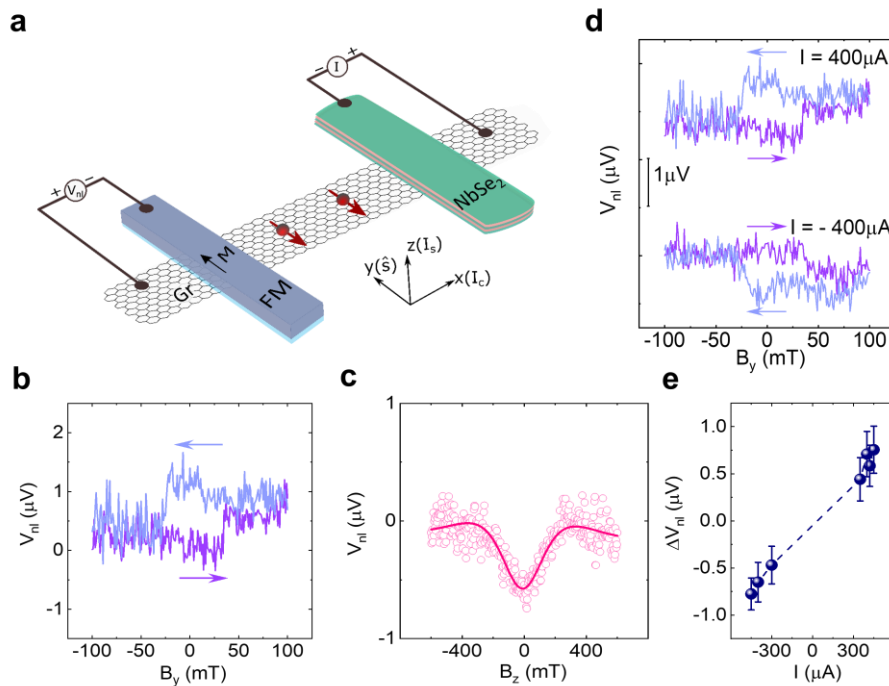


Figure 3. Charge-spin conversion in NbSe₂ at room temperature. (a) Schematic illustration of non-local (NL) measurement geometry to detect the charge-spin conversion effect in NbSe₂ by injecting spin current into the graphene spin channel. (b,c) The spin-switch and Hanle spin precession measurements for spin injection from NbSe₂ with a B_y and B_z sweep, respectively. For spin-switch experiments, the up and down magnetic sweep directions are indicated by arrows. The Hanle data is fitted using equation S1. A linear background is subtracted from the data. (d) Non-local spin-switch signals (V_{nl}) at room temperature with bias currents of $I = \pm 400$ μ A and $V_g = -40$ V. A shift is added in the y-axis for clarity. (e) The magnitude of the spin-switch signal with applied bias

current magnitude in NbSe₂-graphene heterostructure. The error bars are calculated from the noise level of the non-local signal. All the measurements were conducted in Dev 1 at room temperature.

Next, we estimated the spin polarization of NbSe₂ is about $P_{\text{NbSe}_2} = 1 \pm 0.3\%$, assuming the spin polarization of FM contact on bare CVD graphene is $P_{\text{Co}} = 1.5 \pm 0.6\%$ (see Supplementary Note 1)⁵⁶. The efficiency of the CSC process due to spin Hall effect in NbSe₂ can be characterized by the spin Hall angle ($\theta_{\text{SH}} \propto J_s/J_c$) and by using a simple model (as discussed in Supplementary Note 1), we found the θ_{SH} of NbSe₂ varies approximately from 0.68 ± 0.15 to 0.30 ± 0.06 by assuming the variation of spin diffusion length in NbSe₂, $\lambda_{\text{NbSe}_2} = 5 \text{ nm to } 40 \text{ nm}$ (see Fig. S5a and Supplementary Note 2)^{18,57–59}. This estimation of θ_{SH} is consistent with the recently reported theoretical study, where θ_{SH} in NbSe₂ is predicted to be ≈ 0.5 by light irradiation⁶⁰. Note that the spin diffusion length (λ_{NbSe_2}) in NbSe₂ is not experimentally reported yet. We also analytically calculated the length scale, $\theta_{\text{SH}} \cdot \lambda_{\text{NbSe}_2}$ (nm), associated with the CSC in NbSe₂ (5-13nm) (see Fig. S5b), which is comparable to the recently reported length scale in layered TMDCs, e.g., 5nm in WSe₂, 1.15nm in MoTe₂^{15,31}. Another plausible origin of the measured CSC signal could be the Rashba-Edelstein effect (REE) due to Rashba spin-split bands in NbSe₂ and its proximity effect in the NbSe₂-graphene heterostructure region⁵. The characteristic efficiency parameter (α_{RE}) of the REE is calculated (Supplementary Note 2) to be $5.3 \pm 1.8\%$, which is consistent with the recent studies on 2D material heterostructures^{15,24,25,29,30}.

We systematically measured the electrical bias dependence of the CSC signal in NbSe₂, as shown in Fig. 3(d) for the spin-switch signal (V_{nl}). It is evident that reversing the bias current direction results in opposite spin-switch signals due to the reversal of the accumulated spin polarization direction. A full bias-dependent spin-switch measurement was carried out and the amplitudes of the spin-switch signal (ΔV_{nl}) at different bias current magnitudes are summarized in Fig. 3e with a linear fitting (dashed line). It can be seen that with increasing bias current the ΔV_{nl} increases linearly because a larger bias current generates more spin polarization in NbSe₂, which is eventually injected and measured in the graphene spin channel.

Gate dependence of charge to spin conversion signals in NbSe₂

To verify the influence of gate voltage on the CSC signals in NbSe₂ and spin injection into graphene channel, we performed backgate (V_g) dependent measurement of the CSC signals in our devices with the same measurement scheme presented in Fig. 3a. Figure 4a shows the measured non-local spin-switch signals as a function of varying in-plane magnetic field (B_y) at various $V_g = -40 \text{ V to } 50 \text{ V}$ for both n and p doped graphene regime at room temperature. The CSC signals in NbSe₂ and spin injection into graphene are only observed at the higher negative gate voltages. The Hanle spin-precession signals of the CSC effect in our NbSe₂-graphene heterostructure with changing out-of-plane magnetic field (B_z) at different gate voltages are shown in Fig. 4b along with the fitting to equation S1 (solid line). It can be seen that the signals are only also present at the higher negative V_g like spin switch signal.

Figure 4c shows the amplitude of the spin-switch signal, ΔV_{nl} (top panel), and estimated spin lifetime (middle panel), τ_s , of the spin transport in graphene channel after spin is injected from NbSe₂ by CSC process as a function of V_g . To compare the spin transport properties in the graphene channel after the spin is injected from NbSe₂, the NbSe₂-graphene heterostructure channel resistance at different gate voltages is depicted in the bottom panel of Fig. 4c. The Dirac point of the NbSe₂-graphene heterostructure region is about 33V. It can be seen that, when the graphene channel resistance increases for $V_g > -10\text{V}$, the spin injection efficiency decreases due to conductivity mismatch issue between NbSe₂ and graphene⁶¹. The spin transport signal in pristine CVD is shown in Fig. S4c for all the gate voltages in n- and p-doped regimes with a modulation near Dirac point, which can be attributed to the conductivity mismatch between the graphene and the FM contact. The absence of the spin signals,

injected into graphene channel from NbSe₂, at the positive gate voltages can also be due to a strong spin absorption by NbSe₂²⁶.

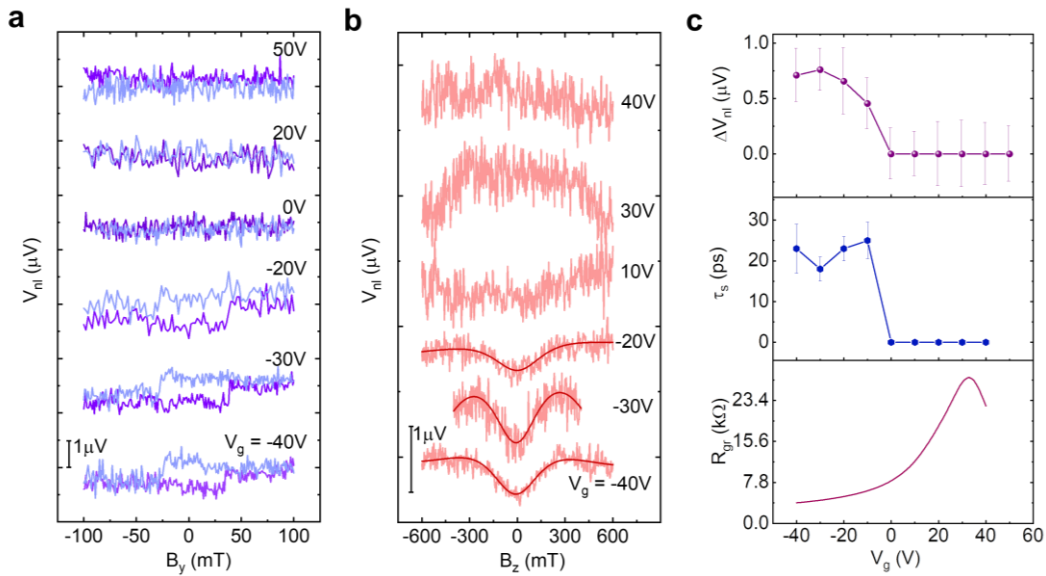


Figure 4: Gate dependence of charge to spin conversion signals in NbSe₂ and spin injection into graphene spin channel. (a) The non-local spin-switch signals as a function of in-plane field (B_y) at various $V_g = -40$ V to 50 V for both n and p doped graphene regime with a constant bias current $I = 400$ μA at room temperature. A linear background has been subtracted from the measured data and y-axis shift is added for clear depiction. (b) The evolution of non-local Hanle spin-precession signals as a function of out-of-plane field (B_z) at various $V_g = -40$ V to 40 V with $I = 420$ μA for both n and p doped graphene regime with fitting to S1 (solid line). (c) The magnitude of the spin-switch signal ΔV_{nl} as a function of V_g (top panel). Error bars are estimated from the noise level of the signal. Back-gate dependence of the spin lifetime (τ_s) of the injected spin in graphene from NbSe₂ (middle panel). Error bars are estimated from the data fitting. The NbSe₂-graphene heterostructure channel resistance at different gate voltages (bottom panel). The measurements were performed in Dev 1 at room temperature.

Temperature dependence of charge-spin conversion in NbSe₂

We measured the temperature dependence of the CSC process in NbSe₂ to observe the evolution of spin polarization in NbSe₂ with temperature in Dev2 (the device picture is shown in Fig. S1d). Figure 5a shows the non-local spin-switch signal arising due to the CSC effect in NbSe₂ and subsequent spin injection into graphene at 3K. The magnitude of the CSC signal is found to be $\Delta R_{nl} \approx 106 \pm 27$ mΩ. Next, we measured the Hanle spin precession signal above and below T_c of NbSe₂ to validate the manifested spin-switch signal is a spin-related phenomenon. Fig. 5b shows the Hanle signals along with the fitting to equation S1. The magnitude of the Hanle spin signal, ΔR_{nl} , and extracted spin lifetime τ_s at different temperatures (3K to 30K) have been shown in Fig. 5c. Interestingly we found that the ΔR_{nl} increases drastically below T_c , but τ_s remains unchanged around 150 ps, below and above T_c , because spin transport parameters of graphene are known to be weakly dependent on temperature^{14,45}. We would like to note that, as τ_s remains unchanged, the larger ΔR_{nl} can be attributed to more efficient CSC conversion effect below T_c . However, the increase in CSC signal with decreasing temperature could also be due to the decrease of NbSe₂ resistivity (ρ_{NbSe_2}) and conductivity mismatch between NbSe₂ and graphene interface.

It is expected that quasiparticle mediated CSC process to be enhanced near the superconducting state of the corresponding material^{35,62}. Besides, the spin lifetime can be extremely high in the SC state of NbSe₂ because it takes a longer time for the quasiparticles to scatter by the spin-orbit impurities in comparison to the normal electron scattering rates^{3,35,36}. Although we manifested CSC signal in NbSe₂ at 3K (below $T_c \sim 7$ K), but we would also like to mention that the NbSe₂ flake is not in the superconducting

state in our CSC experiments as the applied bias current density ($\sim 4 \times 10^6$ A/cm²) is much higher than the critical current density ($\sim 0.7 \times 10^6$ A/cm² at 3K). We optimized the bias current magnitude to maximize the CSC signal at different temperatures that surmount the noise level of the signals, which vary due to the conductivity mismatch of the NbSe₂ and detector FM contact with the graphene spin channel.

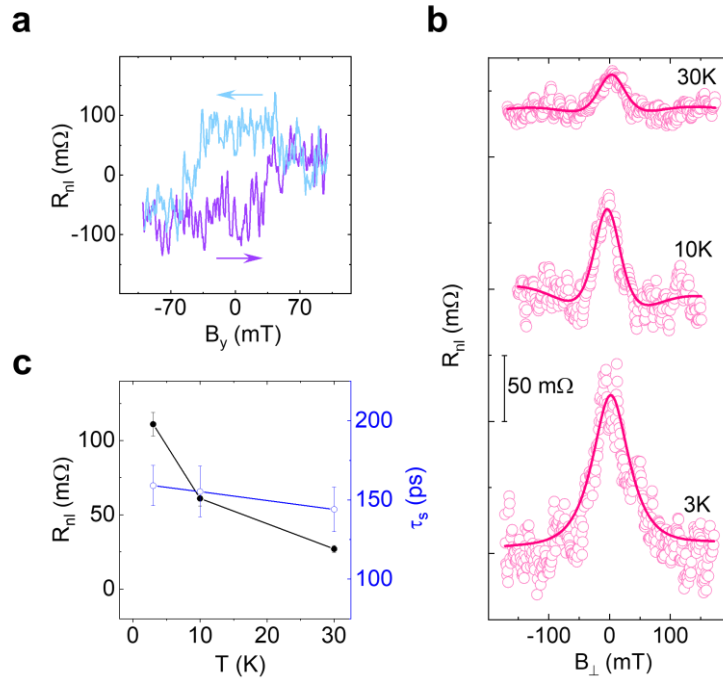


Figure 5. Temperature dependence of charge-spin conversion effect in NbSe₂. (a) Spin-switch signal for charge-spin conversion effect in NbSe₂ (Dev. 2) resulting in spin injection from NbSe₂ into graphene at 3K. (b) Hanle spin precession measurements along with the fitting to equation S1 (solid line). Measurements were performed in Dev 2 in a bias current range of 200 - 500 μ A and at $V_g = -40$ V. A linear background is subtracted from the data and shifted along the y-axis for clear visualization. (c) The magnitude of the Hanle spin signal ΔR_{nl} and extracted spin lifetime (τ_s) at different temperatures.

Discussion

Here, we discuss possible origins that can give rise to the manifested CSC signal in NbSe₂. First and foremost, the non-local spin-switch with varying in-plane B_y field and Hanle spin-precession measurements with changing out-of-plane field B_z confirm that the detected signals are due to the in-plane (y-axis) spin-polarized current that is created in NbSe₂ and injected into graphene^{56,63}. Furthermore, the manifestation of linear bias dependence and a sign reversal behavior with opposite bias current directions rule out the thermal contributions in the measured CSC signal, as the thermal effects should not change with the bias direction and deviate the linear bias dependence^{24,25}. Finally, we can also rule out the spin polarization generation via proximity induced spin Hall effect (SHE) because this effect would have resulted in an out-of-plane spin polarization (s_z) in the heterostructure region, which is not measured⁶⁴. We can also discard the possible impact of the Ising states on the measured CSC signal since Ising spins in the SC state would have turned spin polarization into out of plane (z-axis) direction in NbSe₂, which is not manifested, and our CSC measurements are limited to the non-SC state in NbSe₂. In addition, proximity induced Rashba-Edelstein (REE) effect in graphene from NbSe₂ should have rendered opposite sign of the measured CSC signal for the p- and n-doped regimes^{23,25,30}. However, we observed CSC signal only in the p-doped regime of graphene with higher negative gate voltage, most likely due to the conductivity mismatch issues of the graphene channel with NbSe₂ and FM contacts in the n-doped regime of graphene (see Fig. S2a)^{26,28,61}. Hence, proximity induced REE cannot be ruled out or nor be claimed to be the origin of the observed CSC signal with our measurements. Furthermore, unconventional CSC in NbSe₂ cannot also be disregarded also since NbSe₂ is a layered

material with broken inversion symmetry in the crystal structure, which can be further enhanced by the induced strain at the vdW heterostructure device geometry^{14,15}. Finally, considering the symmetry principle¹⁵, spin polarization direction (s) is set perpendicular to the applied charge current (I_c) and spin current (I_s) direction; the SHE and REE in NbSe₂ most likely merge or independently produce the observed CSC signal in NbSe₂. In future, the measurements of the CSC and inverse CSC in NbSe₂ with different device configurations and measurement geometries with different thicknesses and their correlation with properties in the superconducting state can be interesting.

Summary

We demonstrated CSC in the normal metallic state of NbSe₂ up to room temperature via the spin Hall effect and Rashba Edelstein effect. The engendered spin polarization can be injected into the graphene channel and detected in non-local measurement geometry via spin-switch and Hanle spin precession measurements. The observed gate electric field dependent modulation of the CSC signal in the graphene-NbSe₂ spin-valve device can be due to conductivity mismatch issues or spin absorption processes. Moreover, a higher CSC signal in NbSe₂ is detected at a lower temperature, however, in its non-superconducting state because of the requirement of a higher bias current than the critical current of NbSe₂ for observation of spin signals. Systematic measurements of the spin-switch and Hanle signals reveal that the possible origins of the in-plane spin polarization are predominantly due to the spin Hall effect or Rashba-Edelstein effect in NbSe₂ considering different symmetry-permitted CSC processes. Such features of current-induced spin polarization in NbSe₂ have promising potentials to be used as a non-magnetic spin source in future all-electric spintronic devices and spin-orbit technologies. Furthermore, the realization of CSC in superconducting quantum materials with high SOC strength can enhance the spintronic device performance by generating a larger spin current with a longer spin lifetime^{3,36,65}.

Methods

Device fabrication: To fabricate NbSe₂-graphene heterostructure devices, first, CVD graphene (from Grolltex Inc) stripes were prepared on SiO₂(285 nm)/n-doped Si substrate by electron beam lithography and oxygen plasma etching. NbSe₂ flakes were exfoliated from bulk crystal (from Hq Graphene) by scotch tape and directly transferred onto the CVD graphene channel inside a glovebox in N₂ gas environment. Contacts to graphene and NbSe₂ were defined by electron beam lithography, electron beam evaporation, and the lift-off process. For the preparation of tunnel contacts, first, a total ~1 nm of Ti was evaporated at a base pressure less than 3×10^{-7} Torr and in-situ oxidized for 30 minutes at above 30 Torr. Subsequently, 90 nm of Co was deposited in the same deposition chamber without breaking the vacuum. **Electrical Measurements:** The charge and spin transport measurements are performed in the magneto-transport measurement system and Physical Property Measurement System using a Keithley 6221 current source, a Keithley 2182A nano voltmeter, and Keithley 2612B source meter was used to apply gate voltages.

Acknowledgments

The authors acknowledge financial support from EU Graphene Flagship (Core 3, No. 881603), Swedish Research Council VR project grants (No. 2021-04821), 2D TECH VINNOVA competence center (No. 2019-00068), FLAG-ERA project 2DSOTECH (VR No. 2021-05925), Graphene center, EI Nano, and AoA Materials program at Chalmers University of Technology. We acknowledge the help of staff at Quantum Device Physics and Nanofabrication laboratory in our MC2 department at Chalmers. Devices were fabricated at the Nanofabrication Laboratory, Myfab, MC2, Chalmers.

References

1. Shrivastava, M. & Ramgopal Rao, V. A Roadmap for Disruptive Applications and Heterogeneous Integration Using Two-Dimensional Materials: State-of-the-Art and Technological Challenges. *Nano Lett.* **21**, 6359–6381 (2021).
2. Geim, A. K. & Grigorieva, I. V. Van der Waals heterostructures. *Nature* **499**, 419–425 (2013).
3. Linder, J. & Robinson, J. W. A. Superconducting spintronics. *Nature Physics* **11**, 307–315 (2015).
4. Sinova, J., Valenzuela, S. O., Wunderlich, J., Back, C. H. & Jungwirth, T. Spin Hall effects. *Rev. Mod. Phys.* **87**, 1213–1260 (2015).
5. Manchon, A., Koo, H. C., Nitta, J., Frolov, S. M. & Duine, R. A. New perspectives for Rashba spin-orbit coupling. *Nat. Mater.* **14**, 871–882 (2015).
6. Ahn, E. C. 2D materials for spintronic devices. *npj 2D Materials and Applications* **4**, 1–14 (2020).
7. Roche, S. *et al.* Graphene spintronics: The European Flagship perspective. *2D Materials* **2**, 030202 (2015).
8. Khokhriakov, D., Karpiak, B., Hoque, A. M. & Dash, S. P. Two-dimensional spintronic circuit architectures on large scale graphene. *Carbon N. Y.* **161**, 892–899 (2020).
9. Lin, X., Yang, W., Wang, K. L. & Zhao, W. Two-dimensional spintronics for low-power electronics. *Nature Electronics* **2**, 274–283 (2019).
10. Manipatruni, S. *et al.* Scalable energy-efficient magnetoelectric spin–orbit logic. *Nature* **565**, 35–42 (2019).
11. Guimarães, M. H. D., Stiehl, G. M., MacNeill, D., Reynolds, N. D. & Ralph, D. C. Spin-Orbit Torques in NbSe₂/Permalloy Bilayers. *Nano Lett.* **18**, 1311–1316 (2018).
12. Shi, S. *et al.* All-electric magnetization switching and Dzyaloshinskii–Moriya interaction in WTe₂/ferromagnet heterostructures. *Nature Nanotechnology* **14**, 945–949 (2019).
13. MacNeill, D. *et al.* Control of spin-orbit torques through crystal symmetry in WTe₂/ferromagnet bilayers. *Nat. Phys.* **13**, 300–305 (2017).
14. Zhao, B. *et al.* Unconventional Charge–Spin Conversion in Weyl-Semimetal WTe₂. *Adv. Mater.* **32**, 2000818 (2020).
15. Safeer, C. K. *et al.* Large Multidirectional Spin-to-Charge Conversion in Low-Symmetry Semimetal MoTe₂ at Room Temperature. *Nano Lett.* **19**, 8758–8766 (2019).
16. Stiehl, G. M. *et al.* Layer-dependent spin-orbit torques generated by the centrosymmetric transition metal dichalcogenide β -MoTe₂. *Phys. Rev. B* **100**, 184402 (2019).
17. Ghiasi, T. S., Kaverzin, A. A., Blah, P. J. & Van Wees, B. J. Charge-to-Spin Conversion by the Rashba-Edelstein Effect in Two-Dimensional van der Waals Heterostructures up to Room Temperature. *Nano Lett.* **19**, 5959–5966 (2019).
18. Zhao, B. *et al.* Observation of charge to spin conversion in Weyl semimetal WTe₂ at room temperature. *Phys. Rev. Res.* **2**, 013286 (2020).
19. Sierra, J. F., Fabian, J., Kawakami, R. K., Roche, S. & Valenzuela, S. O. Van der Waals heterostructures for spintronics and opto-spintronics. *Nat. Nanotechnol.* **16**, 856–868 (2021).
20. Wang, Z. *et al.* Origin and magnitude of “designer” spin-orbit interaction in graphene on semiconducting transition metal dichalcogenides. *Phys. Rev. X* **6**, 041020 (2016).
21. Avsar, A. *et al.* Spin-orbit proximity effect in graphene. *Nat. Commun.* **5**, 1–6 (2014).
22. Wang, Z. *et al.* Strong interface-induced spin-orbit interaction in graphene on WS₂. *Nat. Commun.* **6**, 1–7 (2015).
23. Benítez, L. A. *et al.* Tunable room-temperature spin galvanic and spin Hall effects in van der Waals heterostructures. *Nat. Mater.* **19**, 170–175 (2020).
24. Hoque, A. M. *et al.* All-electrical creation and control of spin-galvanic signal in graphene and molybdenum ditelluride heterostructures at room temperature. *Commun. Phys.* **4**, 1–9 (2021).
25. Khokhriakov, D., Hoque, A. M., Karpiak, B. & Dash, S. P. Gate-tunable spin-galvanic effect in graphene-topological insulator van der Waals heterostructures at room temperature. *Nat. Commun.* **11**, 1–7 (2020).
26. Khokhriakov, D. *et al.* Tailoring emergent spin phenomena in Dirac material heterostructures. *Sci. Adv.* **4**, eaat9349

(2018).

27. Kovács-Krausz, Z. *et al.* Electrically Controlled Spin Injection from Giant Rashba Spin-Orbit Conductor BiTeBr. *Nano Lett.* **20**, 4782–4791 (2020).
28. Hoque, A. M., Khokhriakov, D., Karpiak, B. & Dash, S. P. Charge-spin conversion in layered semimetal TaTe₂ and spin injection in van der Waals heterostructures. *Phys. Rev. Res.* **2**, 033204 (2020).
29. Ghiasi, T. S., Kaverzin, A. A., Blah, P. J. & Wees, B. J. van. Charge-to-Spin Conversion by the Rashba–Edelstein Effect in Two-Dimensional van der Waals Heterostructures up to Room Temperature. *Nano Lett.* **19**, 5959–5966 (2019).
30. Li, L. *et al.* Gate-Tunable Reversible Rashba-Edelstein Effect in a Few-Layer Graphene/2H-TaS₂ Heterostructure at Room Temperature. *ACS Nano* **14**, 5251–5259 (2020).
31. Herling, F. *et al.* Gate tunability of highly efficient spin-to-charge conversion by spin Hall effect in graphene proximitized with WSe₂. *APL Mater.* **8**, 071103 (2020).
32. Dvir, T. *et al.* Spectroscopy of bulk and few-layer superconducting NbSe₂ with van der Waals tunnel junctions. *Nat. Commun.* **9**, 1–6 (2018).
33. Khestanova, E. *et al.* Unusual Suppression of the Superconducting Energy Gap and Critical Temperature in Atomically Thin NbSe₂. *Nano Lett.* **18**, 2623–2629 (2018).
34. Staley, N. E. *et al.* Electric field effect on superconductivity in atomically thin flakes of NbSe₂. *Phys. Rev. B - Condens. Matter Mater. Phys.* **80**, 184505 (2009).
35. Wakamura, T. *et al.* Quasiparticle-mediated spin Hall effect in a superconductor. *Nat. Mater.* **14**, 675–679 (2015).
36. Han, W., Otani, Y. C. & Maekawa, S. Quantum materials for spin and charge conversion. *npj Quantum Materials* **3**, 1–16 (2018).
37. Xi, X. *et al.* Ising pairing in superconducting NbSe₂ atomic layers. *Nat. Phys.* **12**, 139–143 (2016).
38. Xing, Y. *et al.* Ising Superconductivity and Quantum Phase Transition in Macro-Size Monolayer NbSe₂. *Nano Lett.* **17**, 6802–6807 (2017).
39. Sohn, E. *et al.* An unusual continuous paramagnetic-limited superconducting phase transition in 2D NbSe₂. *Nat. Mater.* **17**, 504–508 (2018).
40. Bawden, L. *et al.* Spin-valley locking in the normal state of a transition-metal dichalcogenide superconductor. *Nat. Commun.* **7**, 1–6 (2016).
41. Nakata, Y. *et al.* Anisotropic band splitting in monolayer NbSe₂: implications for superconductivity and charge density wave. *npj 2D Mater. Appl.* **2**, 1–6 (2018).
42. Gurram, M., Omar, S. & Van Wees, B. J. Electrical spin injection, transport, and detection in graphene-hexagonal boron nitride van der Waals heterostructures: Progress and perspectives. *2D Materials* **5**, 032004 (2018).
43. Žutić, I., Fabian, J. & Das Sarma, S. Spintronics: Fundamentals and applications. *Rev. Mod. Phys.* **76**, 323–410 (2004).
44. Khokhriakov, D., Karpiak, B., Hoque, A. M. & Dash, S. P. Two-dimensional spintronic circuit architectures on large scale graphene. *Carbon N. Y.* **161**, 892–899 (2020).
45. Kamalakar, M. V., Groenveld, C., Dankert, A. & Dash, S. P. Long distance spin communication in chemical vapour deposited graphene. *Nat. Commun.* **6**, 1–8 (2015).
46. Kamalakar, M. V., Panda, J., Ramu, M., Karis, O. & Sarkar, T. Ultimate spin currents in commercial chemical vapor deposited graphene. *ACS Nano* **14**, 12771–12780 (2020).
47. Gmitra, M., Kochan, D., Högl, P. & Fabian, J. Trivial and inverted Dirac bands and the emergence of quantum spin Hall states in graphene on transition-metal dichalcogenides. *Phys. Rev. B* **93**, 155104 (2016).
48. Gmitra, M. & Fabian, J. Graphene on transition-metal dichalcogenides: A platform for proximity spin-orbit physics and optospintronics. *Phys. Rev. B - Condens. Matter Mater. Phys.* **92**, 155403 (2015).
49. Malard, L. M., Pimenta, M. A., Dresselhaus, G. & Dresselhaus, M. S. Raman spectroscopy in graphene. *Physics Reports* **473**, 51–87 (2009).
50. Wu, Y., An, M., Xiong, R., Shi, J. & Zhang, Q. M. Raman scattering spectra in the normal phase of 2H-NbSe₂. *J. Phys. D. Appl. Phys.* **41**, 175408 (2008).

51. Xi, X. *et al.* Strongly enhanced charge-density-wave order in monolayer NbSe₂. *Nat. Nanotechnol.* **10**, 765–769 (2015).
52. He, X. *et al.* Enhancement of critical current density in a superconducting NbSe₂ step junction. *Nanoscale* **12**, 12076–12082 (2020).
53. Van Tuan, D., Ortmann, F., Cummings, A. W., Soriano, D. & Roche, S. Spin dynamics and relaxation in graphene dictated by electron-hole puddles. *Sci. Rep.* **6**, 21046 (2016).
54. Zhao, B., Hoque, A. M., Khokhriakov, D., Karpiak, B. & Dash, S. P. Charge-spin conversion signal in WTe₂ van der Waals hybrid devices with a geometrical design. *Appl. Phys. Lett.* **117**, 242401 (2020).
55. Karpiak, B. *et al.* 1D ferromagnetic edge contacts to 2D graphene/h-BN heterostructures. *2D Mater.* **5**, 014001 (2017).
56. Garcia, J. H., Vila, M., Cummings, A. W. & Roche, S. Spin transport in graphene/transition metal dichalcogenide heterostructures. *Chemical Society Reviews* **47**, 3359–3379 (2018).
57. Yan, W. *et al.* Large room temperature spin-to-charge conversion signals in a few-layer graphene/Pt lateral heterostructure. *Nat. Commun.* **8**, 1–7 (2017).
58. Savero Torres, W. *et al.* Spin precession and spin Hall effect in monolayer graphene/Pt nanostructures. *2D Mater.* **4**, 041008 (2017).
59. Valenzuela, S. O. & Tinkham, M. Direct electronic measurement of the spin Hall effect. *Nature* **442**, 176–179 (2006).
60. Habara, R. & Wakabayashi, K. Optically induced spin current in monolayer NbSe₂. *Phys. Rev. B* **103**, L161410 (2021).
61. Fert, A. & Jaffrès, H. Conditions for efficient spin injection from a ferromagnetic metal into a semiconductor. *Phys. Rev. B - Condens. Matter Mater. Phys.* **64**, 184420 (2001).
62. Jeon, K.-R. *et al.* Role of Two-Dimensional Ising Superconductivity in the Nonequilibrium Quasiparticle Spin-to-Charge Conversion Efficiency. *ACS Nano* **15**, 16819–16827 (2021).
63. Avsar, A. *et al.* Colloquium : Spintronics in graphene and other two-dimensional materials. *Rev. Mod. Phys.* **92**, 021003 (2020).
64. Safeer, C. K. *et al.* Room-temperature spin hall effect in Graphene/MoS₂ van der waals heterostructures. *Nano Lett.* **19**, 1074–1082 (2019).
65. Eschrig, M. Spin-polarized supercurrents for spintronics. *Phys. Today* **64**, 43–49 (2011).